

Thermal-Dynamics Optimization of Terahertz Quantum Cascade Lasers with Different Barrier Compositions


Martin A. Kainz^{1,2,*}, Moritz Wenclawiak^{1,2}, Sebastian Schönhuber^{1,2}, Michael Jaidl^{1,2}, Benedikt Limbacher^{1,2}, Aaron M. Andrews^{2,3}, Hermann Detz^{2,4}, Gottfried Strasser^{2,3} and Karl Unterrainer^{1,2}

¹Photonics Institute, TU Wien, Vienna 1040, Austria

²Center for Micro- and Nanostructures, TU Wien, Vienna 1040, Austria

³Institute of Solid State Electronics, TU Wien, Vienna 1040, Austria

⁴Central European Institute of Technology, Brno University of Technology, Brno 61200, Czech Republic

 (Received 29 July 2020; revised 25 September 2020; accepted 5 October 2020; published 6 November 2020)

The interplay of high operating temperatures and good heat dissipation is crucial for high-performance terahertz quantum cascade lasers. We therefore study the influence on the cross-plane thermal conductivity of different aluminum concentrations in the barrier of GaAs/Al_xGa_{1-x}As active regions. The thermal conductivity is decreasing from 30 W K⁻¹ m⁻¹ to 12 W K⁻¹ m⁻¹ if the aluminum concentration is increased from 15% to 24%. The temperature during pulsed-laser operation is obtained by measuring the variation of the emission frequency for different laser pulse lengths. This shows, that besides the thermal conductivity, the amount of electric input power has a strong influence on the temperature reached internally during laser operation and is critical for creating high-power devices operating at high temperatures. We show that active regions with thin but high Al_xGa_{1-x}As barriers fulfill this need and are well suited for high-temperature operation. A thermal model of the devices allows prediction of the active-region temperature increase for very short pulse durations. For the structure with 24% Al barriers and a starting temperature of 10 K, the model shows an increase by 24 K for a pulse length of only 300 ns.

DOI: [10.1103/PhysRevApplied.14.054012](https://doi.org/10.1103/PhysRevApplied.14.054012)

I. INTRODUCTION

Quantum cascade lasers (QCLs) [1] are compact electrically driven coherent light sources covering a wide range of wavelengths from the midinfrared to the terahertz (THz) [2]. In the THz regime, the small energy separation between the upper and lower laser state reduces the temperature performance and lasing emission is presently restricted to temperatures below 210 K in pulsed mode [3] and for cw operation a maximum heat-sink temperature (T_{HS}) of 129 K has been demonstrated [4]. To access the full potential of THz QCLs, including spectroscopy and imaging applications, their performance has to be pushed to higher operating temperatures, since this reduces the demand of bulky cryogenic cooling techniques. Recently, first thermoelectric cooled THz QCLs were demonstrated in pulsed operation [3,5], which enables building small cryogenic-free THz setups. However, increasing the temperature performance is still of great importance, since this will increase the optical output power, expand the emission

frequency range, and reduce the size of the thermoelectric cooler, which is needed when aiming towards handheld devices. In recent years, considerable effort has been devoted to increasing the maximum operating temperature of THz QCLs, including different active-region designs [6–8], as well as alternative material systems [9–14]. In a previous study, we investigated the effect of different barrier heights on the maximum operating temperature of GaAs/Al_xGa_{1-x}As THz QCLs [15], where higher barriers lead to higher operating temperatures, resulting from the reduced electron loss into the conduction-band continuum.

It is well known that layered semiconductor heterostructures reduce the cross-plane (in growth direction) thermal conductivity κ_{\perp} [16–21], which is caused by the thermal-boundary resistance (TBR) of the interfaces [22] and influence the thermal management of QCLs. The temperature distribution in the active region of a QCL can be described by the time-dependent heat equation:

$$\nabla \cdot (\kappa_{\perp} \nabla T) + q = \rho c_p \frac{\partial T}{\partial t}, \quad (1)$$

where ρ is the density, c_p the thermal heat capacity at constant pressure, and q the power density. In the case of

*martin.kainz@tuwien.ac.at

steady-state cw operation, κ_{\perp} can be expressed by

$$\kappa_{\perp} = \frac{1}{2} \frac{h}{\Delta T A} P, \quad (2)$$

where h is the height of the active region, A the area of the laser ridge, ΔT the temperature difference between the upper and lower part of the active region, and P is the electrical input power. Equation (2) considers a constant κ_{\perp} through the active region and is therefore a simplified model. Various optical techniques exist to measure the temperature profile of the active region during laser operation, including interferometric thermal mapping [19] and microprobe photoluminescence [20,23], which allow determination of the thermal conductivity.

II. TEMPERATURE-DEPENDENT THERMAL CONDUCTIVITY

In this present study, we investigate how different Al concentrations in the barriers of GaAs/Al_xGa_{1-x}As THz QCLs influence κ_{\perp} , which is highly significant because it determines the possible heat dissipation during laser operation. Two different techniques are used. The first is based on a static measurement, where the temperature of the metallic top waveguide is measured as a function of the electric input power of the QCL structure [21]. To include dynamic effects, the change in refractive index due to increasing temperature during pulsed-laser operation is measured by monitoring the spectral shift of the emitted longitudinal modes [24,25]. The investigated QCL structures consist of a three-well longitudinal-optical-phonon depopulation design and have Al concentrations in the Al_xGa_{1-x}As barriers between 15% and 24% [15]. The static measurement technique uses the change of electrical resistivity in the top metal contact of the ridge waveguide to determine the temperature T_1 of the most upper layer of the active region. We measure the temperature T_2 of a nearby unbiased ridge using the same technique. Due to the different length of the two laser ridges and current crowding effects [26] close to the edges, the temperature distribution at the electrical contacts is not uniform. However, the good thermal conductivity of the substrate GaAs minimizes this effect. Therefore, we can approximate the bottom temperature of the biased ridge to the temperature T_2 . This procedure assures an accurate measurement of the temperature difference ΔT in the active region. The distance of the two laser ridges is 250 μm , which ensures no optical coupling and enables an easy wire bonding of the respective top metal contacts. A schematic of the measurement arrangement is shown in Fig. 1(a). To obtain the temperature calibration curve for each ridge, their electrical resistivity is measured for different T_{HS} using four-terminal sensing.

Figure 1(b) shows the temperature-dependent resistivity for ridge 1 (R_1 : 1 mm \times 120 μm) and ridge 2

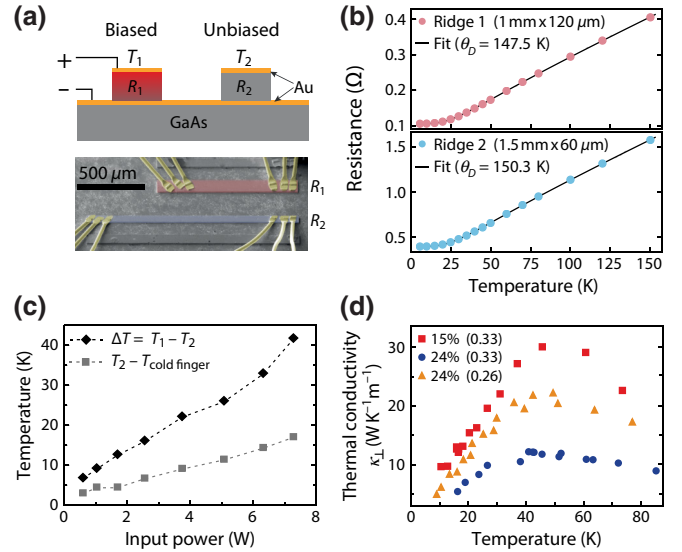


FIG. 1. All-electrical temperature monitoring for THz QCL structures. (a) Schematic of the measurement arrangement, where the temperature difference along the active region of the bias ridge (R_1) is obtained by measuring the temperature of the top contact of two nearby laser ridges. (b) Temperature-dependent resistivity for the two metallic top waveguides. The difference in resistivity for the two ridges is caused by their different width and length. (c) Temperature difference ($T_1 - T_2$) of the biased ridge and temperature difference to the cold finger as a function of the electrical input power to laser ridge R_1 . (d) Temperature-dependent thermal conductivity for different Al concentration with the regarding ratio of barrier and well thicknesses. The temperature on the x axis refers to the average temperature of the bottom and top contact. (c),(d) are measured at a heat-sink temperature of 10 K in cw operation.

(R_2 : 1.5 mm \times 60 μm). It is fitted using the Bloch-Grüneisen model, which describes the relationship of electron-phonon interaction and the electrical resistivity for simple metals [27]. These two calibration curves can further be used to obtain the temperature of the metallic top contact layer for different electrical input powers, which are applied to the QCL structure. Figure 1(c) shows the power-dependent temperature difference $\Delta T = T_1 - T_2$ for the QCL structure with 24% Al barriers, where the input power is applied to laser ridge R_1 for both measurements. ΔT corresponds to the temperature gradient in the active region of the biased QCL ridge. The gray data points represent the temperature difference between the top contact of the unbiased ridge and the cold finger, yielding a thermal resistivity for the cold finger of $R_{\text{th}} = 2.03 \text{ K W}^{-1}$. The temperature difference between T_2 and the cold finger shows that for a precise measurement of the bottom contact of the biased laser ridge the temperature has to be measured close to the operated QCL ridge, which is fulfilled with a distance of 250 μm between R_1 and R_2 . From the observed power-dependent temperature difference $\Delta T(P)$,

the temperature-dependent thermal conductivity $\kappa_{\perp}(T)$ of the active region can be determined by Eq. (2). Figure 1(d) shows $\kappa_{\perp}(T)$ for three different QCL structures. Two structures (red squares and blue circles) have an identical layer sequence but differ in the Al concentration, and one structure (orange triangles) has an Al concentration of 24% but thinner barriers compared to the other two structures [15]. The measurements for all structures show an increase of κ_{\perp} at low temperatures, which is caused by an interplay of boundary scattering [28,29] and a decrease of the TBR at higher temperatures [16,22]. For all structures κ_{\perp} peaks at a temperature around 50 K and the decrease after 50 K is in good agreement with data measured between 75 and 380 K [20], where a continuous decrease of κ_{\perp} was obtained. The fact that the thermal conductivity of a superlattice structure strongly depends on the TBR at the interface reduces the overall thermal conductivity compared to bulk GaAs by a factor approximately equal to 100 [22,28]. The comparison of the 15% structure with the data obtained in Ref. [21] shows a difference in the obtained conductivity. While in the earlier study κ_{\perp} is about $7 \text{ W K}^{-1} \text{ m}^{-1}$, we observe at 20 K a κ_{\perp} of $14 \text{ W K}^{-1} \text{ m}^{-1}$. This difference can be explained by the different heterostructure design, since in Ref. [21] a four-well design was studied. Another reason is based on the different measurement method. Whereas in the earlier study the bottom temperature was set to the cold-finger temperature, we measure this temperature close to the laser ridge, which results in a lower-temperature difference ΔT and hence in a higher κ_{\perp} .

By looking at the two structures with the same layer sequence, the higher Al concentration shows a lower κ_{\perp} , reaching a maximum value of $12 \text{ W K}^{-1} \text{ m}^{-1}$ whereas the structure with 15% Al barriers shows a maximum value of $30 \text{ W K}^{-1} \text{ m}^{-1}$. This is explained by the more pronounced phonon-scattering process for higher Al concentrations, leading to higher TBR [17]. The third structure with 24% Al, but thinner barriers, shows a thermal conductivity, which is located between the values of the other two structures. One would assume a lower value, due to the same material composition as for the other 24% Al structure. However, the shift to higher κ_{\perp} values is due to the thinner barriers compared to the other two structures, which increases phonon tunneling through the barriers [18,30]. Such a structure combines the advantage of high barriers, resulting in a reduced thermal activated electron leakage into the conduction-band continuum [15] and a high thermal conductivity, which is needed for high-temperature THz QCLs operating at high duty cycles [5].

III. TEMPERATURE EVOLUTION DURING PULSED-LASER OPERATION

Like the heterostructures investigated in this work, many other THz QCLs, especially those with high maximum operating temperatures, are restricted to pulsed

operation because their power consumption is too high. Nevertheless, good heat dissipation is very useful for pulsed-laser operation, since it allows the pulse length and repetition rate to be increased, which leads to higher average optical output power. To investigate the heat generation and dissipation during laser operation, we study the temperature-induced frequency shift during pulsed operation, which is caused by the temperature-dependent refractive index of the laser medium [25]. This allows obtaining information about the specific heat capacity c_p , in addition to the measurement of the thermal conductivity. The radiation spectra of the QCLs are measured using an FTIR spectrometer (Bruker Vertex 70) with a spectral resolution of 0.075 cm^{-1} . For the temperature calibration curve, lasing spectra are measured at various temperatures using a short pulse length of 300 ns and a repetition rate of 33.3 kHz (1% duty cycle).

Figure 2(a) shows the obtained spectral response of one lasing mode for a laser device with dimensions of $1 \text{ mm} \times 60 \mu\text{m}$ from the structure with 21% Al barriers between 10 and 140 K. The signal increase for temperatures around 90 K is a special feature of this lasing mode due to the absorption line of residual water vapor in the FTIR spectrometer. For even higher temperatures, the signal is decreasing again due to the temperature-induced decrease of the optical gain. The linewidth of the recorded spectra is limited by the spectral resolution of the FTIR spectrometer. Figure 2(b) shows the center frequency of Gaussian fits for the obtained spectra of the respective lasing mode and shows a clear redshift for higher operating temperatures. This calibration curve can further be used to determine the temperature of the active region (T_{AR}). The slow response of the deuterated triglycine sulfate detector results in a signal, which averages over several different laser pulses. This leads to a spectral broadening for longer pulses, since self-heating during one laser pulse changes the refractive index and therefore causes a redshift of the lasing frequency towards the end of the pulse. By comparing two detected spectra at the same T_{HS} , but different pulse lengths, the change in temperature can be observed. If two short pulses only differ slightly in their pulse length, the measured spectrum of the longer pulse can be approximated by

$$s_2 = s_1 \frac{t_1}{t_2} + g_2, \quad (3)$$

where s_1 and s_2 are the shapes of the detected spectra and t_1 and t_2 are the pulse durations of the shorter and longer pulse, respectively. The factor t_1/t_2 is added to describe the lower repetition rate of the longer pulse keeping a constant duty cycle for both pulse forms. g_2 is the additional term in the spectrum of s_2 caused by the redshift for increased active-region temperature. It has the shape of a Gaussian function with the same width as the Gaussian fits for the

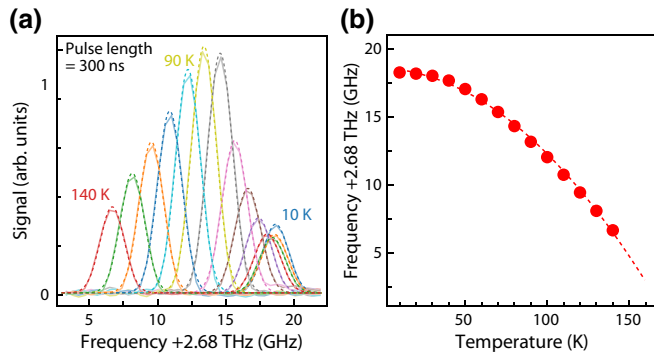


FIG. 2. Dynamic measurement technique. (a) Temperature-dependent frequency shift of a $1 \text{ mm} \times 60 \mu\text{m}$ laser ridge, where the temperature corresponds to the cold-finger temperature T_{HS} . The pulse duration is 300 ns with a repetition frequency of 33.3 kHz (1% duty cycle) and the cold-finger temperature is increased from 10 to 140 K. (b) Center frequencies of Gaussian functions fitted to the obtained spectra. The dashed line is a cubic fit and acts as a temperature calibration curve.

300-ns short pulses shown in Fig. 2(a). The center frequency of this additional function g_2 is determined using a least-squares fit, so that s_2 matches the obtained frequency spectrum for the longer pulse. The temperature at the end of the laser pulse s_2 can be acquired by translating g_2 using the calibration curve shown in Fig. 2(b). This procedure can be repeated for increasing pulse duration and the form of the measured spectra is fitted by

$$s_n = s_{n-1} \frac{t_{n-1}}{t_n} + g_n, \quad (4)$$

where the center frequency of the additional Gaussian function g_n corresponds to the temperature in the time interval $t_n - t_{n-1}$. An illustration of this deconvolution process can be seen in Fig 3(a), which shows the redshift for higher temperatures for short pulse operation and the broadening of the observed spectrum for increased pulse length due to self-heating.

Figures 3(b) and 3(d) show the frequency spectra for different pulse duration at a temperature of 10 and 80 K, respectively. The pulse length is varied from 300 ns to 200 μs and the repetition rate is adapted to have a constant duty cycle of 1%. For the $T_{\text{HS}} = 10 \text{ K}$ measurement a dip in the signal strength around a pulse length of 3 μs is observed, which is a specific feature of this particular lasing mode. A similar behavior is also observed in Fig. 2(b). For $T_{\text{HS}} = 80 \text{ K}$, only a signal decrease is observed, since the maximum signal strength in Fig. 2(a) is observed around 80–90 K. The dashed lines are the functions s_n [see Eq. (4)], where the additional g_n is fitted using a least-squares fit to obtain the best match to the measured spectrum (transparent solid line). The center frequencies of this additional Gaussian function, which corresponds to the lasing frequency of the last section of the pulse, are

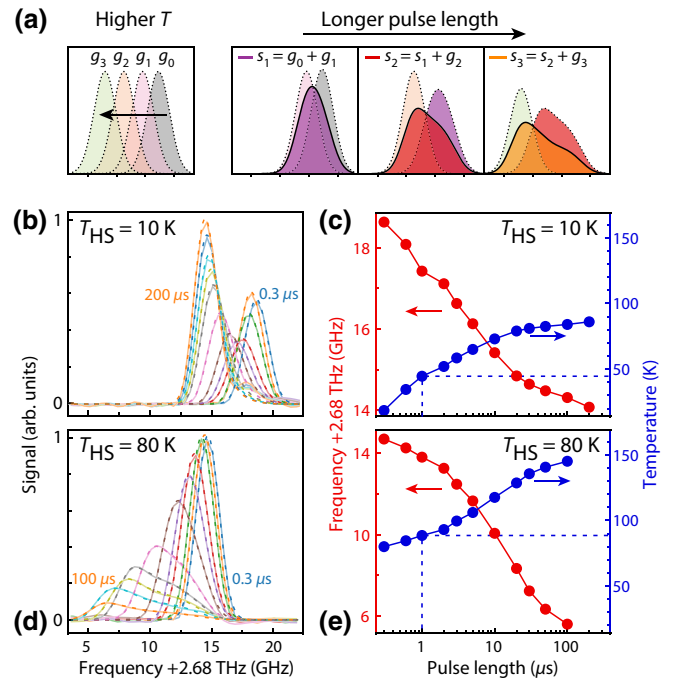


FIG. 3. (a) Illustration of the deconvolution process for widened frequency spectra induced by increased pulse length. (b),(d) Pulse-length-induced frequency shift for T_{HS} of 10 and 80 K, respectively. The repetition rate is adapted for the longer pulse length to maintain a constant duty cycle of 1%. The shape of the recorded radiation spectra is fitted using Eq. (4). (c),(e) The center frequency of g_n , which is the additional Gaussian function to fit the shape of the spectra, is plotted for T_{HS} of 10 and 80 K (red dots) with the corresponding active-region temperature obtained by the calibration curve in Fig. 2(b) (blue dots). The dashed blue lines indicate the temperature after a 1- μs pulse and show a temperature increase of 35 and 9 K for T_{HS} of 10 and 80 K, respectively.

plotted in Figs. 3(c) and 3(e) for the two different T_{HS} (red dots). The calibration curve from Fig. 2(b) is then used to translate the frequencies to the corresponding temperatures (blue dots). For $T_{\text{HS}} = 10 \text{ K}$, the spectra for long pulses saturate at a given frequency and show that T_{AR} approaches a constant value or increases rather slowly. This saturation is caused by an equilibrium of the electric heating and the heat dissipation to the heat sink [compare Eq. (1)]. Surprisingly, for higher T_{HS} , the spectra show a continuous redshift for longer pulses and a decrease of the total intensity. This is a result of the lower dissipated heat at this temperature since κ_{\perp} reduces above 50 K. For the longest pulse of 100 μs , the intensity is reduced roughly by a factor of 2 compared to the spectrum of the 50- μs pulse. After such a long pulse duration, the active region of the QCL reaches the temperature where lasing stops.

The analysis of the temperature increase during various pulse lengths shows a distinct difference for the two T_{HS} . After a pulse duration of 1 μs , the 10-K measurement

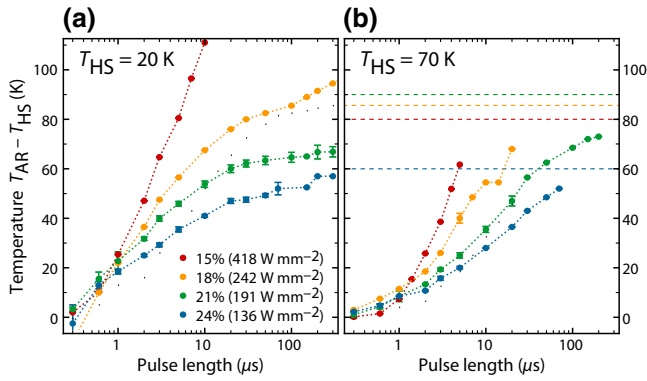


FIG. 4. Measured difference of T_{AR} and T_{HS} during pulsed operation for different Al concentration. (a) Measurement at $T_{HS} = 20$ K. The fast temperature increase in the first μs is caused due to the low heat capacity at low temperatures. The higher current densities for the structure with lower barriers result in a higher electric input power density and therefore also in a stronger increase of T_{AR} , although for these structures the thermal conductivity is higher. (b) The higher specific heat capacity at 70 K results in a lower-temperature increase compared to the 20-K measurement. However, the reduced thermal conductivity leads to a stronger temperature increase for longer pulse duration. The dashed horizontal lines correspond to the maximum lasing temperature of each device.

shows an increase of 35 K, whereas for the 80-K measurement the active region shows only an increase of 9 K [see Figs. 3(c) and 3(e)]. The reason for this difference is the temperature-dependent heat capacity of GaAs, which increases by a factor of 200 from 10 to 100 K [28]. At longer pulse durations, the measurement shows also a different behavior with a lower increase of T_{AR} for low T_{HS} . This can be explained by the maximum value of the thermal conductivity at a temperature of approximately 50 K. Above this value, it decreases again and reduces the thermal heat flow in the active region, which leads to greater increase for the higher T_{HS} .

To compare the temperature evaluation during pulsed operation for different Al compositions in GaAs/ $\text{Al}_x\text{Ga}_{1-x}$ As THz QCLs, the above described measurement is conducted for four structures with identical layer sequence and Al concentrations between 15% and 24% [15]. Figure 4 shows the temperature difference between the heat sink and the active region for two different T_{HS} of 20 and 70 K. For the low-barrier samples (lower Al concentration) a higher temperature difference is observed for both T_{HS} . At a first glance this is unexpected because a higher thermal conductivity has been observed for the lower barriers, which should improve the heat transport and reduce the temperature difference during laser operation. However, the lower barriers increase the current densities and therefore the electrical input power [15]. The results show that the higher input power exceeds the higher thermal conductivity. Particularly in the case of the 15% Al sample,

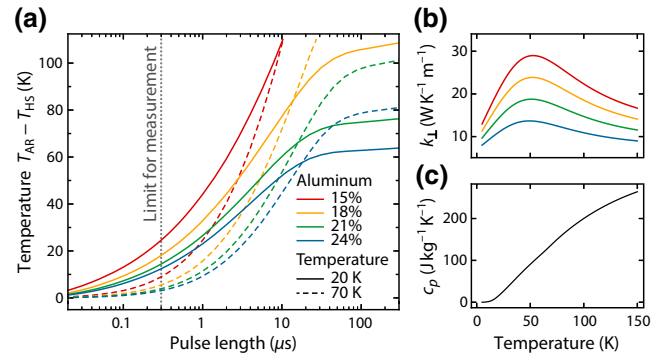


FIG. 5. (a) Simulated temperature increase during one single laser pulse. The temperature increase for long pulse duration is comparable to the measurements shown in Fig. 4. The dashed gray vertical line represents the pulse length of 300 ns, which is used to obtain the temperature calibration curve. The simulation shows, especially for a low T_{HS} and high input power, a strong temperature increase up to this pulse length of 300 ns. (b) The values of $\kappa_{\perp}(T)$ are adapted for the different Al concentrations. (c) $c_p(T)$ of GaAs is taken from Ref. [31].

where the current density at maximum lasing intensity is 1.9 kA cm^{-2} , the temperature increase is very pronounced. For the low T_{HS} , already after a pulse duration of $10 \mu\text{s}$, the active region is heated up close to the critical temperature, where no emission occurs. For all the other structures, lasing emission is observed up to a pulse duration of $300 \mu\text{s}$, where the temperature increase is lower for the higher barrier samples due to the lower current densities. The temperature evolution at a heat-sink temperature of 70 K [see Fig. 4(b)] shows a smaller increase at short pulse duration compared to the 20-K measurement, which is caused by the higher specific heat capacity c_p at higher temperatures. Again, the low-barrier sample shows the highest temperature increase. The structure with 21% Al barriers shows lasing for the longest pulse length of $200 \mu\text{s}$. The maximum lasing temperature T_{max} for all four structures is indicated with dashed horizontal lines, where T_{max} corresponds to the heat-sink temperature where no signal is observed in short pulse operation. For $T_{HS} = 70$ K all structures stop to lase before T_{max} is reached. For long pulse durations the QCLs are not operated at the optimum bias condition, which reduces the optical gain and therefore the maximum operating temperature. With the combination of the two measurement techniques we find that thin and high $\text{Al}_x\text{Ga}_{1-x}$ As barriers are favored for long pulse duration at high-temperature operation, since they reduce electron loss in the continuum [15] and thus the current density and still show decent high thermal conductivity.

To describe the temperature evaluation inside the active region, we perform dynamic heat-transfer simulations using a two-dimensional model. $\kappa_{\perp}(T)$ of the active region is adapted for all Al concentrations [see Fig. 5(b)]. For the

heating source of the different structures, the actual current densities and bias voltages are used. Figure 5(a) shows the simulated temperature increase during one laser pulse for T_{HS} of 20 K (solid) and 70 K (dashed). For long pulses, the simulation reflects quite well the measured temperature evaluation. Interesting is the region at very low pulse durations, which could not be covered by the measurement. For $T_{\text{HS}} = 20$ K, the structure with the highest current density shows for a pulse length of 300 ns already an increase of T_{AR} by 24 K. Due to the higher heat capacity at elevated temperatures [see Fig. 5(c)], this effect is strongly reduced for higher T_{HS} .

IV. CONCLUSION

In conclusion, we study the cross-plane thermal conductivity of different Al concentrations in the barrier of GaAs-based three-well THz QCLs. We show that the more pronounced semiconductor interfaces for higher Al concentrations increase the thermal-boundary resistance and therefore reduce significantly the cross-plane thermal conductivity. Likewise, the thermal resistivity is increased by reducing the thickness of the barrier layers, which results in a structure where the advantage of higher barriers and a good thermal conductivity is combined. To determine the temperature increase of the active region during pulsed-laser operation, we study the lasing spectra for various pulse lengths. A strong influence of the temperature-dependent heat capacity is observed. At low heat-sink temperatures this increases the active-region temperature in the first 1 μs by more than 35 K. Additionally, we show that although the thermal conductivity is higher for lower barriers, the higher current densities result in a stronger increase of the temperature during laser operation. This demonstrates that a balance between high thermal conductivity and decent low current densities is crucial for achieving high-temperature operation of powerful THz QCLs, which can be achieved with higher and thinner $\text{Al}_x\text{Ga}_{1-x}\text{As}$ barriers.

ACKNOWLEDGMENTS

The authors acknowledge financial support from the Austrian Science Fund FWF (DK Solids4Fun W1243, DK CoQuS W1210, and DiPQCL P30709-N27). H.D. acknowledges financial support by the Ministry of Education, Youth and Sports of the Czech Republic under the project CEITEC 2020 (LQ1601) and by the Austrian Agency for International Cooperation in Education and Research (OeAD) within project MULT 01/2020. A.M.A acknowledges funding through COMTERA, a program under the auspices of ERA.NET RUS PLUS (FFG 849614), and AFOSR (FA9550-17-1-0340).

- [1] J. Faist, F. Capasso, D. L. Sivco, C. Sirtori, A. L. Hutchinson, and A. Y. Cho, Quantum cascade laser, *Science* **264**, 553 (1994).
- [2] R. Köhler, A. Tredicucci, F. Beltram, H. E. Beere, E. H. Linfield, A. G. Davies, D. A. Ritchie, R. C. Iotti, and F. Rossi, Terahertz semiconductor-heterostructure laser, *Nature* **417**, 156 (2002).
- [3] L. Bosco, M. Franckić, G. Scalari, M. Beck, A. Wacker, and J. Faist, Thermoelectrically cooled THz quantum cascade laser operating up to 210 K, *Appl. Phys. Lett.* **115**, 010601 (2019).
- [4] M. Wienold, B. Röben, L. Schrottke, R. Sharma, A. Tahraoui, K. Biermann, and H. T. Grahn, High-temperature, continuous-wave operation of terahertz quantum-cascade lasers with metal-metal waveguides and third-order distributed feedback, *Opt. Express* **22**, 3334 (2014).
- [5] M. A. Kainz, M. P. Semsiv, G. Tsianos, S. Kurlov, W. T. Masselink, S. Schönhuber, H. Detz, W. Schrenk, K. Unterrainer, G. Strasser, and A. M. Andrews, Thermoelectric-cooled terahertz quantum cascade lasers, *Opt. Express* **27**, 20688 (2019).
- [6] M. Franckić, L. Bosco, M. Beck, C. Bonzon, E. Mavrona, G. Scalari, A. Wacker, and J. Faist, Two-well quantum cascade laser optimization by non-equilibrium Green's function modelling, *Appl. Phys. Lett.* **112**, 021104 (2018).
- [7] R. W. Adams, K. Vijayraghavan, Q. J. Wang, J. Fan, F. Capasso, S. P. Khanna, A. G. Davies, E. H. Linfield, and M. A. Belkin, GaAs/Al_{0.15}Ga_{0.85}As terahertz quantum cascade lasers with double-phonon resonant depopulation operating up to 172 K, *Appl. Phys. Lett.* **97**, 131111 (2010).
- [8] A. N. Baranov, H. Nguyen-Van, Z. Loghmari, M. Bahriz, and R. Teissier, Terahertz quantum cascade laser with non-resonant extraction, *AIP Adv.* **9**, 055214 (2019).
- [9] L. Ajili, G. Scalari, N. Hoyler, M. Giovannini, and J. Faist, InGaAs–AlInAs/InP terahertz quantum cascade laser, *Appl. Phys. Lett.* **87**, 141107 (2005).
- [10] C. Deutsch, M. Krall, M. Brandstetter, H. Detz, A. M. Andrews, P. Klang, W. Schrenk, G. Strasser, and K. Unterrainer, High performance InGaAs/GaAsSb terahertz quantum cascade lasers operating up to 142 K, *Appl. Phys. Lett.* **101**, 211117 (2012).
- [11] C. Deutsch, M. A. Kainz, M. Krall, M. Brandstetter, D. Bachmann, S. Schönhuber, H. Detz, T. Zederbauer, D. MacFarland, A. M. Andrews, W. Schrenk, M. Beck, K. Ohtani, J. Faist, G. Strasser, and K. Unterrainer, High-power growth-robust InGaAs/InAlAs terahertz quantum cascade lasers, *ACS Photonics* **4**, 957 (2017).
- [12] M. Brandstetter, M. A. Kainz, T. Zederbauer, M. Krall, S. Schönhuber, H. Detz, W. Schrenk, A. M. Andrews, G. Strasser, and K. Unterrainer, InAs based terahertz quantum cascade lasers, *Appl. Phys. Lett.* **108**, 011109 (2016).
- [13] T. Zederbauer, A. Andrews, D. MacFarland, H. Detz, W. Schrenk, and G. Strasser, Enhanced crystal quality of $\text{Al}_x\text{In}_{1-x}\text{As}_y\text{Sb}_{1-y}$ for terahertz quantum cascade lasers, *Photonics* **3**, 20 (2016).
- [14] H. Detz, A. M. Andrews, M. A. Kainz, S. Schönhuber, T. Zederbauer, D. MacFarland, M. Krall, C. Deutsch, M. Brandstetter, P. Klang, W. Schrenk, K. Unterrainer, and G.

- Strasser, Evaluation of material systems for THz quantum cascade laser active regions, *Phys. Status Solidi (a)* **216**, 1800504 (2018).
- [15] M. A. Kainz, S. Schönhuber, A. M. Andrews, H. Detz, B. Limbacher, G. Strasser, and K. Unterrainer, Barrier height tuning of terahertz quantum cascade lasers for high-temperature operation, *ACS Photonics* **5**, 4687 (2018).
- [16] D. G. Cahill, W. K. Ford, K. E. Goodson, G. D. Mahan, A. Majumdar, H. J. Maris, R. Merlin, and S. R. Phillpot, Nanoscale thermal transport, *J. Appl. Phys.* **93**, 793 (2003).
- [17] W. S. Capinski, H. J. Maris, T. Ruf, M. Cardona, K. Ploog, and D. S. Katzer, Thermal-conductivity measurements of GaAs/AlAs superlattices using a picosecond optical pump-and-probe technique, *Phys. Rev. B* **59**, 8105 (1999).
- [18] G. Chen, Thermal conductivity and ballistic-phonon transport in the cross-plane direction of superlattices, *Phys. Rev. B* **57**, 14958 (1998).
- [19] C. Pflügl, M. Litzenberger, W. Schrenk, D. Pogany, E. Gornik, and G. Strasser, Interferometric study of thermal dynamics in GaAs-based quantum-cascade lasers, *Appl. Phys. Lett.* **82**, 1664 (2003).
- [20] M. S. Vitiello, G. Scamarcio, and V. Spagnolo, Temperature dependence of thermal conductivity and boundary resistance in THz quantum cascade lasers, *IEEE J. Sel. Top. Quantum Electron.* **14**, 431 (2008).
- [21] M. Krall, D. Bachmann, C. Deutsch, M. Brandstetter, H. Detz, A. M. Andrews, W. Schrenk, G. Strasser, and K. Unterrainer, All-electrical thermal monitoring of terahertz quantum cascade lasers, *IEEE Photon. Technol. Lett.* **26**, 1470 (2014).
- [22] E. T. Swartz and R. O. Pohl, Thermal boundary resistance, *Rev. Mod. Phys.* **61**, 605 (1989).
- [23] V. Spagnolo, M. Troccoli, G. Scamarcio, C. Gmachl, F. Capasso, A. Tredicucci, A. M. Sergent, A. L. Hutchinson, D. L. Sivco, and A. Y. Cho, Temperature profile of GaInAs/AlInAs/InP quantum cascade-laser facets measured by microprobe photoluminescence, *Appl. Phys. Lett.* **78**, 2095 (2001).
- [24] R. L. Tober, Active region temperatures of quantum cascade lasers during pulsed excitation, *J. Appl. Phys.* **101**, 044507 (2007).
- [25] A. A. Lastovkin, A. V. Ikonnikov, V. I. Gavrilenko, A. V. Antonov, and Y. G. Sadof'ev, Studying the frequency tuning of pulsed terahertz quantum cascade lasers, *Radiophys. Quantum Electron.* **54**, 609 (2012).
- [26] P. Zhang, Q. Gu, Y. Y. Lau, and Y. Fainman, Constriction resistance and current crowding in electrically pumped semiconductor nanolasers with the presence of undercut and sidewall tilt, *IEEE J. Quantum Electron.* **52**, 1 (2016).
- [27] F. Bloch, Zum elektrischen widerstandsgesetz bei tiefen temperaturen, *Zeitschrift für Physik* **59**, 208 (1930).
- [28] R. O. Carlson, G. A. Slack, and S. J. Silverman, Thermal conductivity of GaAs and GaAs_{1-x}P_x laser semiconductors, *J. Appl. Phys.* **36**, 505 (1965).
- [29] J. Callaway, Model for lattice thermal conductivity at low temperatures, *Phys. Rev.* **113**, 1046 (1959).
- [30] P. Hyltdgaard, Resonant thermal transport in semiconductor barrier structures, *Phys. Rev. B* **69**, 193305 (2004).
- [31] J. S. Blakemore, Semiconducting and other major properties of gallium arsenide, *J. Appl. Phys.* **53**, R123 (1982).